PAPER

Check for updates

Temperature-induced structural diversity of metal–organic frameworks and their applications in selective sensing of nitrobenzene and electrocatalyzing the oxygen evolution reaction†

Defang Han,[a] Kun Huang, [ID] *[a] Xianglin Li,[a] Mengni Peng,[a] Linhai Jing,[a] Baoyi Yu,[b] Zeqin Chen*[ac] and Dabin Qin*[a]

Structural diversities are presented in four new Co-MOFs containing 1,5-bi(imidazolyl)anthracene and different dibenzobarrelene skeletons based on dicarboxylic acid, in which MOFs **1–3** exhibit 2D networks in a 4-connected node *sql* topology with the point symbol of $\{4^4 \cdot 6^2\}$, while MOF **4** forms a 1D chain structure. It is clearly observed that the 2D-1D structural transformation of **2–4** has been realized by temperature modulated hydrothermal synthesis procedures from 120–160 °C, suggesting the key role of temperature for constructing MOFs. In addition, obvious π–π interactions between anthracene rings can be observed in the architectures of **1–3**, which may favorably stabilize their 2D supramolecular networks. More importantly, fluorescence behaviors of **1–4** have been investigated in water among various nitro-aromatic compounds (NACs) and the results show that all samples exhibit high selectivity and fine sensitivity to nitrobenzene (NB) with fluorescence quenching, which is confirmed to be the result of electron transfer from the excited state of ligands to that of NB by density functional theory. Furthermore, MOFs **1–4** have been directly employed as electrocatalysts for the oxygen evolution reaction (OER), in which MOF **4** gives the best activity towards the OER among all as-synthesized samples with an overpotential of 398 mV at a current density of 10 mA cm^{-2} and a low Tafel slope of 59 mV dec^{-1}.

Introduction

In the past decades, much attention has been paid to the exploitation of metal–organic frameworks (MOFs), a new class of porous coordination materials, owing to their advantages of tailorable porosity and tunable structures, fantastic topologies, and high surface area,[1] which exhibit excellent performance in fuel gas storage, heterogeneous catalysis, drug delivery system, targeted cancer therapy, luminescent materials and so on.[2] Generally, the application of MOFs largely depends on their architectural features. As a result, it is a great challenge and of significance to adopt a new synthetic method in preparing MOFs with targeted architectures and expected properties. In an earlier report, multidentate ligands, including multi-imidazole and multi-carboxylate, have been used as building blocks for constructing MOFs with fascinating structures, novel topologies and varieties of applications.[2c,3] In addition, to make full utilization of the coordination sites in imidazole/carboxylate, mixed ligands of them have been employed for the construction of various functional MOFs, which achieves remarkable progress in tailoring structures and improving properties.[4] However, the structural formation of MOF may suffer from several factors, such as temperature, metal centers, organic linkers, solvent, and so on.[5] Among them, temperature plays key role for the formation of structural mold, and different temperature can lead to the diversity of MOFs from the same starting materials. Besides, the utilization of several aromatic rings contained rigid ligands in construction of MOFs may contribute to stable frameworks *via* π-stacking interactions among aromatic rings,[6] which are also considered easily to predict the final topologies compared to that of the flexible ligands[1b,7] Meanwhile, introduction of aromatic π-rings in organic ligands may enhance the host-guest chemical interactions between the analytes and

[a] Key Laboratory of Chemical Synthesis and Pollution Control of Sichuan Province, School of Chemistry and Chemical Engineering, China West Normal University, Nanchong 637002, P. R. China. E-mail: hkun2017@cwnu.edu.cn; qdbkyl@cwnu.edu.cn

[b] Key Laboratory of Urban Agriculture (North China), Ministry of Agriculture, College of Biological Sciences Engineering, Beijing University of Agriculture, Beijing 102206, P. R. China

[c] College of Materials and Chemistry and Chemical Engineering, Chengdu University of Technology, Chengdu, 610059, P. R. China. E-mail: chenzeqin@sina.com

MOFs in chemical sensing.[3e,8] As far as we know, there are some examples for constructing MOFs with the same metal core involving rigid hybrid ligands of multi-imidazole and multi-carboxylate, however, the researches on the relationship between the architectures and temperature are rather rare.[5a–g]

Up to date, a great variety of MOFs have been applied in chemical sensing *via* the interactions between the target analyst and the porosity/surface area of MOFs.[9] Particularly, chemical sensing based on the fluorescence changes is considered as a simple, sensitive and rapid method for recognizing ions, molecules and so on. Recently, developing MOF-based chemical sensors for detection of NACs attracts extensive attention owing to the high explosiveness and hazardousness of NACs, which are of great significance for public security and environmental protection.[10] As a member of NACs, NB is widely used as solvent and intermedia in chemical synthesis, which gradually causes concerns for its environmental pollution. Though several examples of MOFs-based sensors have been reported with sensing ability towards NB,[11] to our knowledge, most of them suffered from interferences caused by other NACs and thus showed low selectivity to NB among variety of NACs (Table S1†).[11a–h] Consequently, it is highly desirable to explore efficient MOF-based sensors that can detect NB with high selectivity and sensitivity by fluorescent response. On the other hand, developing efficient electrocatalysts for oxygen evolution reaction (OER) presents as an attractive strategy in clean energy generation and storage.[12] Actually, OER is generally considered to baffle the electrocatalytic water splitting due to its kinetically sluggish, low efficiency, poorly structural stability and *etc.*[13] As such, to utilize proper and highly efficient catalysts in electricity-driven systems for water splitting to produce oxygen is significant and challenging. For the reasons mentioned above, MOFs have emerged as a class of promising electrocatalytic catalysts owing to their advantages in porous structure, active surface area, and open metal sites, which may facilitate the enhancement of catalytic activity. So far, enormous MOF-based catalysts have been designed and developed with excellent OER activities, some of which could comparably with non-precious metal electrocatalysts, displaying great potentials for developing electrocatalytic OER materials.[14] Nevertheless, developing MOF based electrocatalysts for OER is still in its infant stage, especially, a limited number of pristine MOFs have been reported for direct use in catalytic OER. Therefore, exploring low-cost but efficient pristine MOF electrocatalysts for OER is significant and challenging.

In consideration of the aforementioned as well as our continuous research for development and application of MOFs, herein, mixed organic ligands including rigid 1,5-bi(imidazolyl)anthracene and dibenzobarrelene skeletons based dicarboxylic acid were introduced to construct a series of luminescent 2D/1D Co-MOFs (1–4) for the first time (Scheme 1). Meanwhile, a facile method *via* varying temperature to tailor the structures of MOFs has been conducted successfully during the hydro-thermal processes. Then the luminescent behaviors of all prepared MOFs were systematically investigated, which showed obvious solvent-dependent fluorescent spectra and exhibited high selectivity and fine sensitivity towards NB among various NACs by fluorescence quenching. Moreover, the
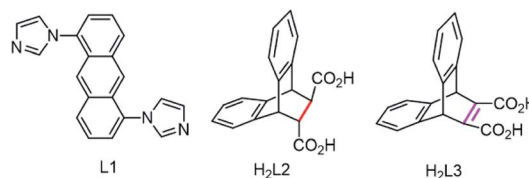
Scheme 1 The structures of bidentate imidazole ligand **L1** and dibenzobarrelene based carboxylic acid ligands **H₂L2** and **H₂L3**.

specific response to NB was further demonstrated by density functional theory (DFT) calculations. Significantly, MOFs **1–4** have been directly employed as electrocatalysts for oxygen evolution reaction (OER), in which MOF **4** showed the best activity towards OER among all as-synthesized samples, achieving overpotential of 398 mV at current density of 10 mA cm⁻² and Tafel slope of 59 mV dec⁻¹. We anticipate this work can shed light on fabricating MOFs with structural diversity *via* temperature regulation and applying MOFs in sensing and electrocatalytic OER materials.

Experimental

Materials and methods

All chemicals were obtained from Aladdin (Shanghai) or Chengdu Kelong Chemical Co., Ltd. (Chengdu). **H₂L2** and **H₂L3** were synthesized according to the previous method.[15] NMR spectra were recorded on a Bruker advance II 400 MHz NMR spectrometer. All FT-IR absorption spectroscopy were obtained from a Nicolet 6700 with KBr pellets. X-ray powder diffractions were collected by Rigaku Dmax/Ultima IV diffractometer. Thermogravimetric analyses (TGA) were obtained from a Netzsch STA 449 F3 thermal analyzer. Elemental analyses were acquired from a PerkinElmer 240 elemental analyzer. Nitrogen adsorption isotherms were recorded at 77 K *via* Autosorb-IQ gas analyzer. Brunauer–Emmett–Teller (BET) method was employed for evaluating the specific surface area and pore size distribution. Fluorescence measurements were conducted on a Cary Eclipse fluorescence spectrophotometer. Electrochemical activities of **1–4** for OER were examined using a CHI-660E electrochemical workstation equipped with a standard three electrode system.

Synthesis of 1,5-bi(imidazolyl)anthracene (L1). To a dry DMF (20 mL) solution of imidazole (5.0 g, 73.5 mmol) in a 100 mL two-necked flask were wadded NaH (3.0 g, 125.0 mmol), which were stirred at room temperature for 0.5 h, followed by addition of 1,5-dichloroanthracene (1 g, 4.1 mmol) and CuI (0.57 g, 3.0 mmol) under N₂ atmosphere. The resulting mixture was heated to 140 °C for 48 hours and cooled to room temperature. After that, the reaction mixture was poured into 100 mL water and extracted with CH₂Cl₂ (50 mL × 3). The combined organic layers were dried over anhydrous Na₂SO₄ and evaporated to remove the solvent. The residue was purified by column chromatography to obtain the target product in 40% yield (0.5 g). Mp: 260–262 °C ¹H NMR (400 MHz, DMSO-d₆) δ 8.35 (s, 2H), 8.26–8.22 (m, 2H), 8.10 (s, 2H), 7.69 (s, 1H), 7.66–7.63 (m, 4H), 7.29 (s, 2H).¹³C NMR (100 MHz, DMSO-d₆) δ 138.59, 133.65,

132.16, 129.70, 129.20, 127.55, 125.59, 124.07, 122.14, 121.99. Anal. calcd (%) for $C_{20}H_{14}N_4$: C, 90.29; H, 4.51; N, 20.6; found: C, 90.40; H, 4.50; N, 20.56. HRMS calcd m/z 311.1297 for $[M + H]^+$, found m/z 311.1309 for $[M + H]^+$.

Synthesis of $\{[Co_2(L1)_2(L2)_2 \cdot (H_2O)_2]_n \cdot 3H_2O\}$ (1). A mixture of **L1** (15.5 mg, 0.05 mmol), **H$_2$L2** (14.7 mg, 0.05 mmol) and $Co(NO)_3 \cdot 6H_2O$ (29.1 mg, 0.1 mmol) were dissolved in a mixture solution of CH_3CN (2 mL) and H_2O (6 mL), which was heated to 120 °C with a heating rate of 3 °C min^{-1} and reacted for 96 h in a 20 mL Teflon vial. Then the reaction was cooled down to room temperature to obtain purplish red block crystals in 72% yield (based on **L1** ligand). Elemental analysis (%), calcd for $C_{76}H_{62}Co_2N_8O_{13}$: C, 64.53; H, 4.38; N, 7.92; found: C, 63.72; H, 4.46; N, 7.83.

Synthesis of $\{[Co_2(L1)_2(L3)_2 \cdot (H_2O)_2]_n \cdot 4H_2O\}$ (2). To a mixture of **L1** (15.5 mg, 0.05 mmol) and **H$_2$L3** (29.2 mg, 0.1 mmol) in CH_3CN/H_2O solution (8 mL, v/v = 1/3) were added $Co(NO)_3 \cdot 6H_2O$ (29.1 mg, 0.1 mmol), which were heated to 120 °C at a heating rate of 3 °C min^{-1} in a Teflon vial and reacted for 96 hours. After cooled to room temperature, brownish blocks crystals of **2** were obtained in 48% yield (based on **L1** ligand). Elemental analysis (%), calcd for $C_{76}H_{60}Co_2N_8O_{14}$: C, 63.90; H, 4.20; N, 7.85; found: C, 63.87; H, 4.23; N, 7.84.

Synthesis of $\{[Co(L1)_2(HL3)_2]_n \cdot 2CH_3CN\}$ (3). The prepared procedure was according to that of **2** except for altering the heating temperature to 140 °C. Brown block crystals of complex **3** were collected in 56% yield (based on **L1** ligand). Elemental analysis (%), calcd for $C_{80}H_{56}CoN_{10}O_8$: C, 71.41; H, 4.17; N, 10.42; found: C, 71.47; H, 4.18; N, 10.38.

Synthesis of $\{[Co(L1)(HL3)_2 \cdot (H_2O)_2]_n\}$ (4). The synthetic method was according to that of **2** only by altering the heating temperature to 160 °C. Brown block crystals of **4** were obtained in 26% yield (based on **L1** ligand). Elemental analysis (%), calcd for $C_{56}H_{40}CoN_4O_{10}$: C, 68.09; H, 4.08; N, 5.67; found: 68.06; H, 4.09; N, 5.65.

Crystallographic data collection and refinement. The crystal data for **1–4** were collected on a Bruker SMART APEX-II CCD diffractometer with graphite monochromatic Mo-Kα radiation (λ = 0.71073 Å) by using the ω-scan technique at 293 °C. All structures were solved by direct methods and refined with the full-matrix least-squares procedures on F^2 using the SHELXL-97 (ref. 16) and Olex-2 programs, respectively. All H atoms were generated geometrically at idealized positions at idealized positions and refined using the riding model. The CCDC deposition numbers allocated to **1–4** were 1887850, 1887851, 1887854 and 1887855, respectively. Topology analyses were carried out by using TOPOS program.[17] Corresponding data for **1–4** were provided in Tables 1, S2 and Fig. S1.†

Results and discussion

L1 was synthesized by a modified C–N coupling under the catalyst of CuI in about 40% yield as depicted in Scheme S1.†[3a] **H$_2$L2** and **H$_2$L3** were facilely prepared in a high yield *via* Diels–Alder reaction and ester hydrolysis process according to

literature.[12] **L1** was characterized by NMR spectra and HRMS (Fig. S1–S3†). MOFs **1–4** were characterized by FT-IR spectra (Fig. S4†).

$\{[Co_2(L1)_2(L2)_2 \cdot (H_2O)_2]_n \cdot 3H_2O\}$ (1)

The single crystal X-ray data reveals complex **1** conforms to the triclinic crystal system, space group $P\bar{1}$. Fig. 1a shows an asymmetric unit of **1** containing two Co(II) atoms: Co1 and Co2, in which Co1 is six-coordinated by two nitrogen atoms from **L1** and four oxygen atoms from two carboxylate ligands **H$_2$L2** in μ-bridged mode,[4b] while Co2 forms an octahedral geometry by coordinating to two oxygen atoms from two carboxylate ligands **H$_2$L2**, two oxygen atoms from two water molecules, and two nitrogen atoms from two **L1** molecules, respectively. Subsequently, Co1 and Co2 are connected by two oxygen atoms from a carboxylate ligand, which further coordinate to N atoms form **L1** to form a 2D structure. Interestingly, π–π stacking interactions between anthracene rings can be observed with face to face distances of 3.5377–3.5661 Å, which contribute to the formation of a 2D net structure (Fig. 1b and c). The structure of compound **1** can be simplified by topology program as a 2D square grid network with the point symbol of $\{4^4 \cdot 6^2\}$ (Fig. 1d).

$\{[Co_2(L1)_2(L3)_2 \cdot (H_2O)_2]_n \cdot 4H_2O\}$ (2)

Structural analysis reveals that complex **2** belongs to a triclinic crystal system with the space group of $P\bar{1}$. Fig. 2a shows the asymmetry unit of **2** contains two six-coordinated Co(II) cations (Co1 and Co2) with octahedral geometry, respectively, in which Co1 connects with four oxygen atoms from two **L3** ligands and two nitrogen atoms from ligands **L1**, while Co2 coordinates to two oxygen atoms from two lattice water, two oxygen atoms form two carboxylate ligands and two N atoms from **L1**. Co1 and Co2 are bridged by carboxylate ligand, which further links to **L1** ligands respectively to form a 2D network. Meanwhile, strong face to face π–π stacking interactions between the anthracene rings can be observed with face to face distances of about 3.4946–3.5291 Å, which may be favorably for the formation of 2D structure (Fig. 2b and c). Topological analysis shows complex **2** can be simplified as a 4-connected node *sql* with a Schläfli symbol of $\{4^4 \cdot 6^2\}$ (Fig. 2d).

$\{[Co(L1)_2(HL3)_2]_n \cdot 2CH_3CN\}$ (3)

Single-crystal X-ray data shows that complex **3** crystallized in the monoclinic system with space group $P2_1/c$. The secondary building unit (SBU) is consisted by two **HL3**$^-$, one Co(II) and four **L1** ligands to present an octahedral geometry as depicted in Fig. 3a. The connections between Co(II) atoms and **L1** further leads to the formation of a 2D network, in which extensive distorted face to face π-stacking interactions can be observed with contribution to the self-assembly of 2D supramolecular structure (face to face distances of about 3.8205 Å) (Fig. 3b and c). Topologically, MOF **3** can be depicted as a 4-connected node with the point symbol $\{4^4 \cdot 6^2\}$ (Fig. 3d). The coordination environment of Co(II) in SUB of MOF **3** is different to that of **2**, providing the evidence for temperature-induced diversities of structure.

Table 1 Crystallographic data for MOFs **1–4**

Compounds	**1**	**2**	**3**	**4**
Formula	$C_{76}H_{62}Co_2N_8O_{13}$	$C_{76}H_{60}Co_2N_8O_{14}$	$C_{80}H_{56}CoN_{10}O_8$	$C_{56}H_{40}CoN_4O_{10}$
fw	1431.9	1427.18	1344.27	987.85
Temp., K	293(2)	293.15	293(2)	293(2)
Crystal syst	Triclinic	Triclinic	Monoclinic	Monoclinic
Space group	$P\bar{1}$	$P\bar{1}$	$P2_1/c$	$P2_1/n$
a (Å)	10.353(4)	10.336(8)	14.1122(9)	13.407(6)
b (Å)	12.285(6)	12.301(10)	27.0471(18)	12.528(4)
c (Å)	14.373(5)	14.368(11)	9.1595(7)	15.550(10)
α (deg)	101.162(12)	101.18(2)	90	90
β (deg)	107.318(10)	107.255(19)	108.227(2)	114.216(19)
γ (deg)	107.004(13)	107.055(19)	90	90
V (Å^3)	1588.1(11)	1587(2)	3320.7(4)	2382(2)
Z	1	1	2	2
D_c (g cm^{-3})	1.478	1.493	1.344	1.377
μ (mm^{-1})	0.599	0.601	0.326	0.427
R_{int}	0.0395	0.0633	0.0589	0.0749
Reflections collected/unique	5818/4860	5811/4495	7367/5696	4872/3436
GOF on F^2	1.028	1.063	1.029	1.041
$R_1{}^a$, $wR_2{}^b$ [$I > 2\sigma(I)$]	0.0334/0.0824	0.0464/0.1195	0.0422/0.0937	0.0443/0.0968
$R_1{}^a$, $wR_2{}^b$ (all data)	0.0439/0.0876	0.0668/0.1307	0.0644/0.1035	0.0773/0.1099
Largest peak, hole (e Å^{-3})	0.30/−0.33	0.81/−0.62	0.41/-0.30	0.23/−0.34

^{a} $R_1 = \sum||F_o| - |F_c||/\sum|F_o|$. ^{b} $wR_2 = \sum[w(F_o{}^2 - F_c{}^2)^2]/\sum[w(F_o{}^2)^2]^{1/2}$.

$\{[Co(L1)(HL3)_2\cdot(H_2O)_2]_n\}$ (4)

Structural analysis shows that complex **4** is a monoclinic crystal system, space group $P2_1/n$. The asymmetric SBU has a six coordinated Co(II) core connecting with two O atoms from two **HL3** ligands, two N atoms form two **L1** and two O atoms from two lattice water molecules to form a octahedral geometry (Fig. 4a), in which the another N atom of imidazole in **L1** further coordinates to Co(II) in next SBU, forming a 1D chain structure (Fig. 4b and c), further suggesting the key role of temperature in the synthesis of MOF.

It is worth noting that ligands variation in synthetic processes lead to a slight pore size change from micropore in **1** to mesoporous in **2**, which may due to the more rigid dibenzobarrelene derived carboxylate ligand **H₂L3** (bridgehead C=C) compared to that of **H₂L2** (bridgehead C–C), while no other obvious structural changes between them can be observed. However, temperature controlled strategies employed in synthetic processes of MOFs **2–4** causes the distinct coordination environment of Co(II) (two coordination modes of dibenzobarrelene derived carboxylate ligands as depicted in Scheme S2†) as well as the transformation from 2D porous structure (**2** and **3**) to 1D chain structure (**4**) with a gradual rise in temperature. The above mentioned results imply the important roles of ligands/temperature in tailoring structure of MOFs.

PXRD, TGA and N₂ adsorption

Fig. S5† shows the experimental PXRD patterns of MOFs **1–4** closely match that simulated patterns obtained from the single crystal data, demonstrating the phase purity of as-synthesized MOFs. As depicted in Fig. S6,† TG curves for **1–4** were
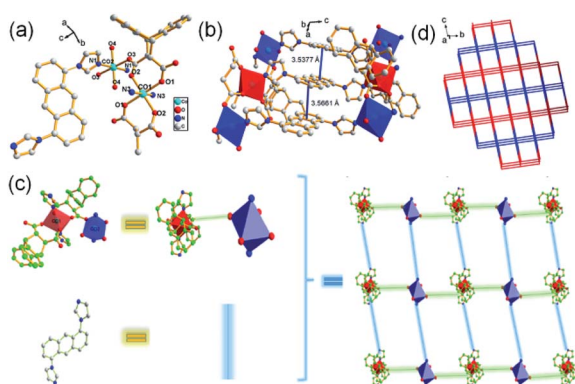

Fig. 1 (a) Asymmetric unit of **1**, symmetry code: (i) = 1 − x, 1 − y, 1 − z; (ii) = 2 − x, 1 − y, 1 − z; (iii) = 2 − x, 1 − y, 2 − z; (iv) = 1 − x, 1 − y, −z; (b) π-stacking interactions in **1**; (c) simplified 2D structure of **1**; (d) topology structure of **1**.
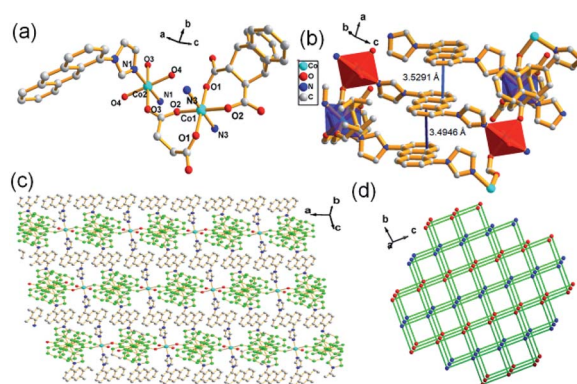

Fig. 2 (a) Asymmetric unit of **2**, symmetry code: (i) = 2 − x, 1 − y, 2 − z; (ii) = 1 − x, 1 − y, 2 − z; (iii) = 1 − x, 1 − y, 1 − z; (iv) = 2 − x, 1 − y, 1 − z; (b) π-stacking interactions between the anthracene rings in **2**; (c) 2D structure of **2**; (d) topological analysis of **2**.
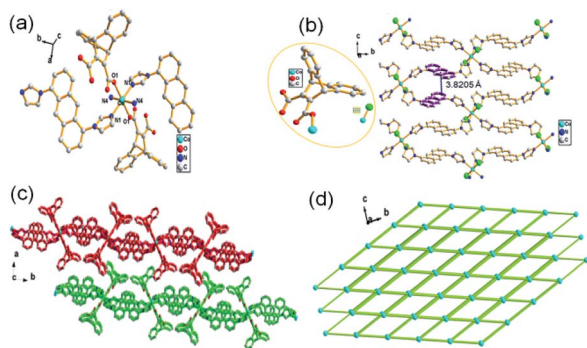
Fig. 3 (a) The SBU of **3**, symmetry code: (i) = −x, 1 − y, −z; (ii) = +x, 3/2 − y, 1/2 + z; (iii) = −x, −1/2 + y, −1/2 − z; (iv) = −x, 1/2 + y, −1/2 − z; (b) infinite 2D layer of **3**; (c) stack-configuration of **3**; (d) topological architecture of **3**.

recorded in the temperature range of 35–600 °C to evaluate the stability of samples. Based on the thermogravimetric analysis, complex **1** loses 2.8% (calcd 2.5%) weight from 150–180 °C associated with the loss of crystallization water, which begins to collapse beyond *ca.* 270 °C. Complex **2** has a weight loss of 3.3% (calcd 2.5%) from 100–228 °C, corresponding to the water molecules, and then decomposes around 270 °C. A weight loss of 6.7% (calcd 6.1%) is observed when complex **3** is heated from 35–270 °C, which should be ascribed to the escape of residual acetonitrile molecule, and a structural decomposition occurs at about 280 °C. For complex **4**, it exhibits a weight loose of 3.5% (calcd 3.6%) between 100–250 °C corresponding to the lattice water, which begins to collapse at around 251 °C. The results demonstrate the good stability of these samples. In addition, the porous structures of **1**–**3** were evaluated by N_2 adsorption at 77 K. Fig. S7† shows BET surface areas of complex **1**–**3** are estimated to be 13.694 $m^2 g^{-1}$, 10.485 $m^2 g^{-1}$ and 4.194 $m^2 g^{-1}$, respectively. Meanwhile, the pore diameters of them are calculated to be 1.754 nm, 2.000 nm, and 3.502 nm, respectively.

Sensing behaviors towards nitrobenzene

To understand the luminescent behaviors of MOFs **1**–**4**, 0.3 mg of them were added respectively into 3 mL suitable solvents and ultrasonated for 0.5 h to obtain dispersed suspensions. Firstly, the emission profiles of **1**–**4** were investigated in different solvents. Fig. S8† show all samples present obvious emission peaks centered at the range of 400–430 nm, while they show almost completely quenching phenomena with nearly 100% quenching efficiency in NB, which is analogues to that of most

reported MOFs.[11i–m] Though a slight solvation effect for the wavelength can be observed with different solvents polarity, suggesting solvent-dependence of the emission intensity, no obvious relationship between them can be found. Secondly, to further investigate the selectivity of these MOFs towards NB among various NACs, water was chosen as detection medium for its environment friendliness. Then the specific responses of MOFs towards nitrobenzene among various NACs were examined in water under 270 nm excitation by fluorescence spectra, in which the suspension solutions of **1**–**4** were added with equivalents of different NACs including NB, 4-hydroxynitrobenzene (4-NP), 2,4,6-trinitrophenol (TNP), 2-nitrophenol (2-NP), 1-chloro-4-nitrobenzene (4-CNB), 4-nitrotoluene (4-NTol), 2-nitro-phenylamine (2-NPA), 3-nitrophenol (3-NP), 2,4-dinitroaniline (2,4-DNA), 4-nitroaniline (4-NPA), 2,4-dinitrophenylhydrazine (2,4-NPH) and 4-nitrobenzoic acid (4-NBA). Fig. S9† and 5 show samples **1**–**4** exhibit obvious fluorescence bands centered at *ca.* 425 nm, and the addition of low concentrations (1.7×10^{-5} mol L^{-1}) of NB causes significant decreases in fluorescence intensity at 425 nm with quenching efficiencies of 60.0%, 76.6%, 75.5% and 68.3% for MOFs **1**–**4**, respectively, while the other NACs only elicit slight decreases in emission intensity with quenching efficiency less than 20%. The results indicate all MOFs show high selectivity towards nitrobenzene compared with that of other MOF-based sensors in Table S1,† which may be ascribed to PET process from the ligands to NB.[11a] In addition, the effect of other NACs for the specific responses of MOFs **1**–**4** towards NB were evaluated by competition experiments, in which the fluorescence profiles were obtained from the chemosensors solutions in the presence of various NACs coexisting with NB, respectively. Fig. 6 exhibits other NACs causes no obvious fluorescence changes of **1**–**4** compared to that of NB alone, further suggesting the high selectivity of these MOFs towards NB. To better understand the sensing behaviors of **1**–**4** towards NB, the fluorescence titration assays of them were recorded by treatment of increasing concentrations of NB, respectively. As can be seen from Fig. 7, low concentration of NB (3.3 μM) can trigger obvious fluorescence changes for all samples, indicating their sensitivities towards NB. Overall, the fluorescence intensity of all MOFs
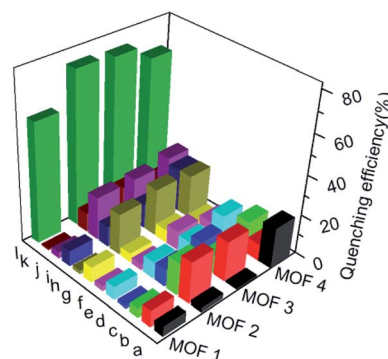

Fig. 4 (a) The SBU of **4**, symmetry code: (i) = 1 − x, −y, 1 − z; (ii) = −x, −y, 1 − z; (b) 1D chain structure of **4**; (c) stacking diagram of **4**.

Fig. 5 Emission quenching efficiencies of **1**–**4** in water after the addition of various NACs (16.7 μM). Histograms (a)–(l) represent: 4-NP; TNP; 2-NP; 4-CNB; 4-NTol; 2-NPA; 3-NP; 2,4-DNA; 4-NPA; 2,4-NPH; 4-NBA and NB, respectively.
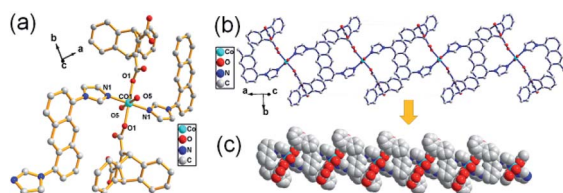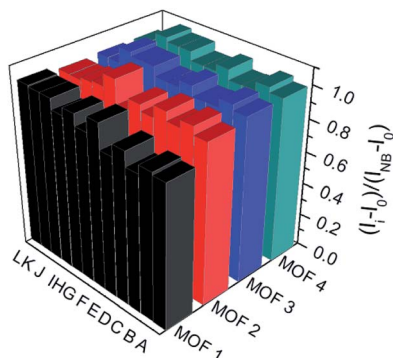
Fig. 6 Emission intensity ratio changes of MOFs **1–4** towards NB (16.7 μM) and NB (16.7 μM) in presence of equivalent other NACs. Histogram (A)–(L) represent: NB + 4-NP; NB + TNP; NB + 2-NP; NB + 4-CNB; NB + 4-NTol; NB alone; NB + 2-NPA; NB + 3-NP; NB + 2, 4-DNA; NB + 4-NPA; NB + 2, 4-NPH and NB + 4-NBA, respectively.

sharply decreases with the addition of NB below the concentrations of *ca.* 16.7 μM and completely quenches at high concentration of NB (*ca.* 70 μM) with quenching efficiencies beyond 96%. The fluorescence quenching efficiency is evaluated *via* Stern–Volmer formula $(I_0/I) = K_{sv} [NB] + 1$, where I_0 and I represent the fluorescence intensity before and after addition of an NB, respectively; ([NB] refers to the concentration of NB, and K_{sv} is the quenching constant). Fig. S9† shows a linear increase in the S–V plots at the low concentrations of NB, while the further increasing concentration causes divergences from the linearity, which could be probably ascribed to an analogous diffusion-controlled energy transfer process reported in literature.[11l] Moreover, the K_{sv} values of **1–4** for NB are evaluated as 4.59×10^4 M^{-1}, 6.15×10^4 M^{-1}, 3.28×10^4 M^{-1} and 4.50×10^4 M^{-1}, respectively, which are larger than that in the previous literatures.[11j,k] Besides, MOFs **1–4** can be renewable and reused for four numbers of cycles *via* centrifugation, filtration and rinsing several times with DMF, which show insignificant

quenching efficiency decreases after four repeated cycles, suggesting the stability and recyclability of MOFs **1–4** in detection of NB (Fig. S11†).

Considering either the porous frameworks of **1–3** (1.754 nm, 2.000 nm and 3.502 nm for **1–3**, respectively) or 1D structure of **4** could provide suitable pores for inclusion of NB molecule (6.0 Å), the possible quenching mechanism is suggested to be the electron transfer processes from the electron donating ligands to the electron deficient NB molecules that adhered to the surface of MOFs.[18] With the above idea in mind as well as to further illustrate the specific response mechanisms of MOFs **1–4** to NB, the fluorescence quenching mechanism was examined at the level of B3LYP/6-31G* according to density functional theory. Fig. 8 shows the LUMO (−3.1026 eV) of NB is lower than that of ligands **H₂L2**, **H₂L3** and **L1** (−0.9954 ev, −2.3454 ev and −1.1685 ev, respectively), which is favorable for electron transfer from the excited state of ligands to that of NB, resulting in luminescence quenching behaviors. As state above, all prepared MOF samples exhibit high selectivity towards NB *via* PET mechanism controlled fluorescence quenching process.

Electrocatalytic OER

Electrocatalytic properties of MOFs **1–4** were investigated. Fig. 9a shows the polarization curves of all as-synthesized samples obtained by LSV measurements, in which **1–4** present electrocatalytic OER activities with onset overpotentials of 354, 352, 373 and 345 mV, and overpotentials of 411, 406, 438 and 398 mV for achieving current density of 10 mA cm^{-2} (η_{10}), respectively. The results could compare favorably to those of OER catalysts in reported works (Table S3†).[14d,e] Fig. 9b shows OER kinetics of MOFs **1–4** are characterized with Tafel plots of 58, 62, 60, and 59 mV dec^{-1}, respectively, revealing a more favorable kinetics of **4** for electrocatalytic OER. Next, electrochemical impedance spectroscopy (EIS) was conducted to evaluate the electrode activities for OER under operating conditions. As shown in Fig. S12,† all MOFs deliver more than one semicircles in the Nyquist curves. The low frequency loop may be attributed to the adsorption on the electrode surface of reaction intermediate such as O$_{ad}$ as reported in literature,[14e] and the high frequency loop corresponds to charge transfer
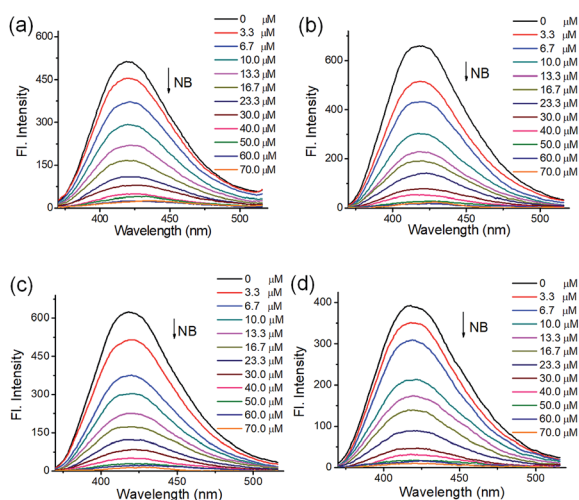

Fig. 7 Emission profiles of MOFs ((a–d) for **1–4**, respectively) upon treatment of different concentrations of NB (0–70 μM) in water, λ_{ex}: 270 nm.
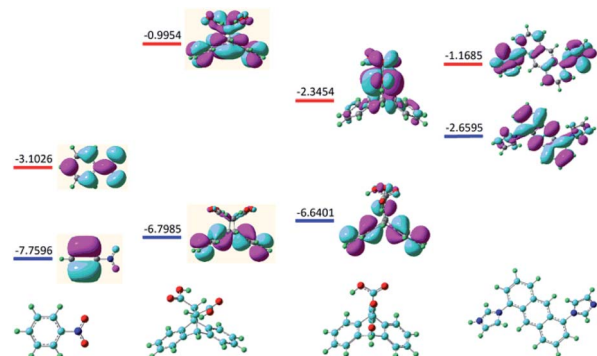

Fig. 8 Optimal structures and calculated HOMO (blue) and LUMO (red) orbits for NB and ligands **H₂L2**, **H₂L3** and **L1**.
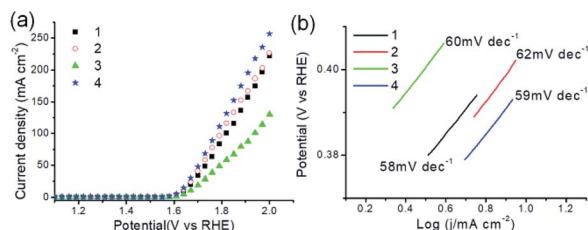
Fig. 9 (a) OER polarization curves of as-synthesized MOFs **1–4** in 1 M KOH solution with a scan rate of 5 mV s^{-1}. (b) Tafel plots of **1–4**.

processes. Among them, **4** holds the smallest value of charge-transfer resistance (R_{ct}), revealing the fastest electron transfer property and high electrocatalytic activity toward oxygen production under the catalysis of **4**. Furthermore, the PXRD patterns of **1–4** immersed in 1 M KOH for 2 h were acquired. As provided in Fig. S13,† the PXRD patterns of all samples remain almost unchanged, suggesting their retained crystallinity and stabilities. As described, MOFs **1–4** exhibit promising activities for electrocatalytic OER.

Conclusions

In conclusion, four 2D/1D Co-MOFs have been designed and obtained with structural diversities based on 1,5-biimidazoylanthracene and different dibenzobarrelene skeletons derived dicarboxylic acid, among which **1–3** show 2D network in a 4-connected node *sql* with the point symbols of $\{4^4 \cdot 6^2\}$ and **4** presents a 1D chain structure. Notably, strategy of varying temperature to tailor the structures of MOFs have been adopted and realized in the synthesis of **2–4**, suggesting the key role of temperature in constructing MOFs. In addition, MOFs **1–4** exhibit high selectivity and sensitivity towards NB among various nitro-aromatics compounds in water, which is confirmed to be a result of electron transfer from the excited state of ligands to that of NB by density functional theory. Besides, MOFs **1–4** can be directly used as electrocatalysts for OER and **4** exhibits the best activity among all as-synthesized samples with low overpotential of 398 mV to achieve current density of 10 mA cm^{-2} and Tafel slope of 59 mV dec^{-1}. This work is of great importance for extensively developing structural diversity MOFs *via* temperature regulation and employing MOFs as efficiently sensing and electrocatalytic materials.

Conflicts of interest

There are no conflicts to declare.

Acknowledgements

Notes and references

1 (*a*) M. Eddaoudi, H. Li and O. M. Yaghi, *J. Am. Chem. Soc.*, 2000, **122**, 1391–1397; (*b*) X. C. Huang, Y. Y. Lin, J. P. Zhang and X. M. Chen, *Angew. Chem., Int. Ed.*, 2006, **45**, 1557–1559; (*c*) O. K. Farha, I. Eryazici, N. C. Jeong, B. G. Hauser, C. E. Wilmer, A. A. Sarjeant, R. Q. Snurr, S. T. Nguygn, A. O. Yazaydin and J. T. Hupp, *J. Am. Chem. Soc.*, 2012, **134**, 15016–15021; (*d*) J. Pang, S. Yuan, J. Qin, C. Liu, C. Lollar, M. Wu, D. Yuan, H. C. Zhou and M. Hong, *J. Am. Chem. Soc.*, 2017, **139**, 16939–16945; (*e*) X. Gu and D. Xue, *CrystEngComm*, 2007, **9**, 471–477.

2 (*a*) H. Furukawa, K. E. Cordova, M. O'Keeffe and O. M. Yaghi, *Science*, 2013, **341**, 1230444; (*b*) B. Chen, N. W. Ockwig, A. R. Millward, D. S. Contreras and O. M. Yaghi, *Angew. Chem., Int. Ed.*, 2005, **44**, 4745–4749; (*c*) Z. Zhou, C. He, J. Xiu, L. Yang and C. Duan, *J. Am. Chem. Soc.*, 2015, **137**, 15066–15069; (*d*) P. Horcajada, R. Gref, T. Baati, P. K. Allan, G. Maurin, P. Couvreur, C. Férey, R. E. Morris and C. Serre, *Chem. Rev.*, 2012, **112**, 1232–1268; (*e*) M. X. Wu and Y. W. Yang, *Adv. Mater.*, 2017, **29**, 1606134; (*f*) J. Park, Q. Jiang, D. Feng, L. Mao and H. C. Zhou, *J. Am. Chem. Soc.*, 2016, **138**, 3518–3525; (*g*) S. Khatua, S. Goswami, S. Biswas, K. Tomar, H. S. Jena and S. Konar, *Chem. Mater.*, 2015, **27**, 5349–5360; (*h*) J. X. Hou, J. P. Gao, J. Liu, X. Jing, L. J. Li and J. L. Du, *Dyes Pigm.*, 2019, **160**, 159–164; (*i*) G. Xiong, B. Yu, J. Dong, Y. Shi, B. Zhao and L. N. He, *Chem. Commun.*, 2017, **53**, 6013–6016.

3 (*a*) L. Luo, P. Wang, G. C. Xu, Q. Liu, K. Chen, Y. Lu, Y. Zhao and W. Y. Sun, *Cryst. Growth Des.*, 2012, **12**, 2634–2645; (*b*) H. J. Lee, P. Y. Cheng, C. Y. Chen, J. S. Shen, D. Nandi and H. M. Lee, *CrystEngComm*, 2011, **13**, 4814–4816; (*c*) Z. Wei, Z. Y. Gu, R. K. Arvapally, Y. P. Chen, R. N. McDougald Jr, J. F. Ivy, A. A. Yakovenko, D. Feng, M. A. Omary and H. C. Zhou, *J. Am. Chem. Soc.*, 2014, **136**, 8269–8276; (*d*) J. Pang, C. Liu, Y. Huang, M. Wu, F. Jiang, D. Yuan, F. Hu, K. Su, G. Liu and M. Hong, *Angew. Chem., Int. Ed.*, 2016, **55**, 7478–7482; (*e*) M. Zhang, Z. Qi, Y. Feng, B. Guo, Y. Hao, Z. Xu, L. Zhang and D. Sun, *Inorg. Chem. Front.*, 2018, **5**, 1314–1320; (*f*) A. K. Crane, N. G. White and M. J. MacLachlan, *CrystEngComm*, 2015, **17**, 4912–4918; (*g*) T. Wang, K. Huang, M. Peng, X. Li, D. Han, L. Jing and D. Qin, *CrystEngComm*, 2019, **21**, 494–501.

4 (*a*) W. G. Yuan, F. Xiong, H. L. Zhang, W. Tang, S. F. Zhang, Z. He, L. Jing and D. Qin, *CrystEngComm*, 2014, **16**, 7701–7710; (*b*) Y. Liang, W. G. Yuan, S. F. Zhang, Z. He, J. Xue, X. Zhang, L. Jing and D. Qin, *Dalton Trans.*, 2016, **45**, 1382–1390; (*c*) C. H. Ke, G. R. Lin, B. C. Kuo and H. M. Lee, *Cryst. Growth Des.*, 2012, **12**, 3758–3765; (*d*) S. Q. Zang, M. M. Dong, Y. J. Fan, H. W. Hou and T. C. Mak, *Cryst. Growth Des.*, 2012, **12**, 1239–1246; (*e*) S. F. Zhang, F. Xiong, Z. He, Y. Liang, J. R. Xue, L. H. Jing and D. B. Qin, *Polyhedron*, 2015, **102**, 401–409; (*f*) S. Mukherjee, D. Samanta and P. S. Mukherjee, *Cryst. Growth Des.*, 2013, **13**, 5335–5343; (*g*) L. Luo, S. Q. Liu, X. W. Xu, J. Xu and J. L. Zhao, *CrystEngComm*, 2018, **20**, 7719–7728.

5 (a) B. Liu, L. Wei, N. N. Li, W. P. Wu, H. Miao, Y. Y. Wang and Q. Z. Shi, *Cryst. Growth Des.*, 2014, **14**, 1110–1127; (b) H. F. Zhou, T. He, K. F. Yue, Y. L. Liu, C. S. Zhou, N. Yan and Y. Y. Wang, *Cryst. Growth Des.*, 2016, **16**, 3961–3968; (c) L. Y. Du, H. Wang, G. Liu, D. Xie, F. S. Guo, L. Hou and Y. Y. Wang, *Dalton Trans.*, 2015, **44**, 1110–1119; (d) B. Zheng, H. Dong, J. Bai, Y. Li, S. Li and M. Scheer, *J. Am. Chem. Soc.*, 2008, **130**, 7778–7779; (e) Y. B. Dong, Y. Y. Jiang, J. Li, J. P. Ma, F. L. Liu, B. Tang, R. Q. Huang and S. R. Batten, *J. Am. Chem. Soc.*, 2007, **129**, 4520–4521; (f) K. L. Gurunatha, K. Uemura and T. K. Maji, *Inorg. Chem.*, 2008, **47**, 6578–6580; (g) P. Cui, L. Ren, Z. Chen, H. Hu, B. Zhao, W. Shi and P. Cheng, *Inorg. Chem.*, 2012, **51**, 2303–2310; (h) X. Y. Duan and M. L. Wei, *Cryst. Growth Des.*, 2017, **17**, 1197–1207; (i) J. J. Hou, X. Q. Li, P. Gao, H. Q. Sun and X. M. Zhang, *Cryst. Growth Des.*, 2017, **17**, 3724–3730; (j) Y. F. Hou, B. Liu, K. F. Yue, C. S. Zhou, Y. M. Wang, N. Yan and Y. Y. Wang, *CrystEngComm*, 2014, **16**, 9560–9567.

6 (a) Z. He, K. Huang, F. Xiong, S. F. Zhang, J. R. Xue, Y. Liang, L. H. Jing and D. B. Qin, *J. Organomet. Chem.*, 2015, **797**, 67–75; (b) X. J. Li, Z. J. Yu, T. N. Guan, X. X. Li, G. C. Ma and X. F. Guo, *Cryst. Growth Des.*, 2014, **15**, 278–290.

7 (a) M. Eddaoudi, J. Kim, N. Rosi, D. Vodak, J. Wachter, M. O'Keeffe and O. M. Yaghi, *Science*, 2002, **295**, 469–472; (b) N. B. Shustova, A. F. Cozzolino and M. Dincǎ, *J. Am. Chem. Soc.*, 2012, **134**, 19596–19599.

8 M. Zhang, L. Zhang, Z. Xiao, Q. Zhang, R. Wang, F. Dai and D. Sun, *Sci. Rep.*, 2016, **6**, 20672.

9 (a) Z. Hu, B. J. Deibert and J. Li, *Chem. Soc. Rev.*, 2014, **43**, 5815–5840; (b) W. P. Lustig, S. Mukherjee, N. D. Rudd, A. V. Desai, J. Li and S. K. Ghosh, *Chem. Soc. Rev.*, 2017, **46**, 3242–3285; (c) Y. Zhang, S. Yuan, G. Day, X. Wang, X. Yang and H. C. Zhou, *Coord. Chem. Rev.*, 2018, **354**, 28–45.

10 (a) S. S. Nagarkar, B. Joarder, A. K. Chaudhari, S. Mukherjee and S. K. Ghosh, *Angew. Chem., Int. Ed.*, 2013, **52**, 2881–2885; (b) C. Wang, J. Shang, Y. Lan, T. Tian, H. Wang, X. Chen, J. Y. Gu, J. Z. Liu, L. J. Wan, W. Zhu and G. Li, *Adv. Funct. Mater.*, 2015, **25**, 6009–6017; (c) M. Bagheri, M. Y. Masoomi, A. Morsali and A. A. Schoedel, *ACS Appl. Mater. Interfaces*, 2016, **8**, 21472–21479; (d) R. B. Fu, S. M. Hu and X. T. Wu, *J. Mater. Chem. A*, 2017, **5**, 1952–1956.

11 (a) S. Pramanik, C. Zheng, X. Zhang, T. J. Emge and J. Li, *J. Am. Chem. Soc.*, 2011, **133**, 4153–4155; (b) J. H. Qin, B. Ma, X. F. Liu, H. L. Lu, X. Y. Dong, S. Q. Zang and H. Hou, *Dalton Trans.*, 2015, **44**, 14594–14603; (c) W. Xie, S. R. Zhang, D. Y. Du, J. S. Qin, S. J. Bao, J. Li, Z. M. Su, W. W. He, Q. Fu and Y. Q. Lan, *Inorg. Chem.*, 2015, **54**, 3290–3296; (d) L. Li, S. Zhang, L. Xu, L. Han, Z. N. Chen and J. Luo, *Inorg. Chem.*, 2013, **52**, 12323–12325; (e) L. Di, J. J. Zhang, S. Q. Liu, J. Ni, H. Zhou and Y. J. Sun, *Cryst. Growth Des.*, 2016, **16**, 4539–4546; (f) S. Zhang, L. Han, L. Li, J. Cheng, D. Yuan and J. Luo, *Cryst. Growth Des.*, 2013, **13**, 5466–5472; (g) X. Zhou, H. Li, H. Xiao, L. Li, Q. Zhao, T. Yang, J. Zuo and W. Huang, *Dalton Trans.*, 2013, **42**, 5718–5723; (h) Y. N. Gong, L. Jiang and T. B. Lu, *Chem. Commun.*, 2013, **49**, 11113–11115; (i) G. Y. Wang, L. L. Yang, Y. Li, H. Song, W. J. Ruan, Z. Chang and X. H. Bu, *Dalton Trans.*, 2013, **42**, 12865–12868; (j) R. X. Yao, X. Cui, X. X. Jia, F. Q. Zhang and X. M. Zhang, *Inorg. Chem.*, 2016, **55**, 9270–9275; (k) Y. T. Yan, J. Liu, G. P. Yang, F. Zhang, Y. K. Fan, W. Y. Zhang and Y. Y. Wang, *CrystEngComm*, 2018, **20**, 477–486; (l) D. M. Chen, X. Z. Ma, W. Shi and P. Cheng, *Cryst. Growth Des.*, 2015, **15**, 3999–4004; (m) D. Liu, X. Liu, Y. Liu, Y. Yu, F. Chen and C. Wang, *Dalton Trans.*, 2014, **43**, 15237–15244.

12 C. Tan and H. Zhang, *Chem. Soc. Rev.*, 2015, **44**, 2713–2731.

13 (a) S. Piccinin, A. Sartorel, G. Aquilanti, A. Goldoni, M. Bonchio and S. Fabris, *Proc. Natl. Acad. Sci. U. S. A.*, 2013, **110**, 4917–4922; (b) W. Zhang and K. Zhou, *Small*, 2017, **13**, 1700806; (c) S. Wang, Y. Hou, S. Lin and X. Wang, *Nanoscale*, 2014, **6**, 9930–9934.

14 (a) J. Q. Sheng, P. Q. Liao, D. D. Zhou, C. T. He, J. X. Wu, W. X. Zhang, J. P. Zhang and X. M. Chen, *J. Am. Chem. Soc.*, 2017, **139**, 1778–1781; (b) Y. T. Xu, Z. M. Ye, J. W. Ye, L. M. Cao, R. K. Huang, J. X. Wu, D. D. Zhou, X. F. Zhang, C. T. He, J. P. Zhang and X. M. Chen, *Angew. Chem., Int. Ed.*, 2019, **131**, 145–149; (c) J. Duan, S. Chen and C. Zhao, *Nat. Commun.*, 2017, **8**, 15341; (d) F. Dai, W. Fan, J. Bi, P. Jiang, D. Liu, X. Zhang, H. Lin, C. Gong, R. Wang, L. Zhang and D. Sun, *Dalton Trans.*, 2016, **45**, 61–65; (e) J. Jiang, L. Huang, X. Liu and L. Ai, *ACS Appl. Mater. Interfaces*, 2017, **9**, 7193–7201; (f) X. Zhao, B. Pattengale, D. Fan, Z. Zou, Y. Zhao, J. Du, J. Huang and C. Xu, *ACS Energy Lett.*, 2018, **3**, 2520; (g) J. Li, W. Huang, M. Wang, S. Xi, J. Meng, K. Zhao, J. Jin, W. Xu, Z. Wang, X. Liu, Q. Chen, L. Xu, X. Liao, Y. Jiang, A. K. Owusu, B. Jing, C. Chen, D. Fan, L. Zhou and L. Mai, *ACS Energy Lett.*, 2018, **4**, 285–292; (h) Z. Xue, Y. Li, Y. Zhang, W. Geng, B. Jia, J. Tang, S. Bao, H. Wang, Y. Fan, Z. Wei, Z. Zhang, Z. Ke, G. Li and C. Su, *Adv. Energy Mater.*, 2018, **8**, 1801564; (i) F. L. Li, Q. Shao, X. Huang and J. P. Lang, *Angew. Chem., Int. Ed.*, 2018, **57**, 1888–1892; (j) W. Zhou, D. D. Huang, Y. P. Wu, J. Zhao, T. Wu, J. Zhang, D. S. Li, C. Su, P. Feng and X. Bu, *Angew. Chem., Int. Ed.*, 2019, **58**, 1–6; (k) G. Hai, X. Jia, K. Zhang, X. Liu, Z. Wu and G. Wang, *Nano Energy*, 2018, **44**, 345–352; (l) S. Zhao, Y. Wang, J. Dong, C. T. He, H. Yin, P. An, K. Zhao, X. Zhang, C. Gao, L. Zhang, J. Lv, J. Wang, J. Zhang, A. M. Khattak, N. A. Khan, Z. Wei, J. Zhang, S. Liu, H. Zhao and Z. Tang, *Nat. Energy*, 2016, **1**, 16184; (m) K. Wan, J. Luo, C. Zhou, T. Zhang, J. Arbiol, X. Lu, B. W. Mao, X. Zhang and J. Fransaer, *Adv. Funct. Mater.*, 2019, **29**, 1900315; (n) X. Zhang, J. Luo, K. Wan, D. Plessers, B. Sels, J. Song, L. Chen, T. Zhang, P. Tang, J. R. Morante, J. Arbiol and J. Fransaer, *J. Mater. Chem. A*, 2019, **7**, 1616–1628.

15 İ. Çapan and S. Servi, *Synth. Commun.*, 2018, **48**, 1164–1171.

16 G. M. Sheldrick, *Acta Crystallogr., Sect. A: Found. Crystallogr.*, 2008, **64**, 112–122.

17 V. A. Blatov, A. P. Shevchenko and V. N. Serezhkin, *J. Appl. Crystallogr.*, 2000, **33**, 1193.

18 (a) B. Gole, A. K. Bar and P. S. Mukherjee, *Chem. Commun.*, 2011, **47**, 12137–12139; (b) J. S. Qin, S. J. Bao, P. Li, W. Xie, D. Y. Du, L. Zhao, Y. Q. Lan and Z. M. Su, *Chem.–Asian J.*, 2014, **9**, 749–753.